JACS
JOURNAL OF THE AMERICAN CHEMICAL SOCIETY
Article
pubs.acs.org/JACS

Spectroscopic and DFT Characterization of a Highly Reactive Nonheme Fe^{V}–Oxo Intermediate

Ruixi Fan,[†] Joan Serrano-Plana,[‡,#] Williamson N. Oloo,[§,⊗] Apparao Draksharapu,[§] Estefanía Delgado-Pinar,[⊥] Anna Company,[‡] Vlad Martin-Diaconescu,[‡] Margarida Borrell,[‡] Julio Lloret-Fillol,[∥] Enrique García-España,*[,⊥] Yisong Guo,*[,†] Emile L. Bominaar,*[,†] Lawrence Que, Jr.,*[,§] Miquel Costas,*[,‡] and Eckard Münck*[,†]

[†]Department of Chemistry, Carnegie Mellon University, 4400 Fifth Avenue, Pittsburgh, Pennsylvania 15213, United States
[‡]Grup de Química Bioinspirada, Supramolecular i Catálisi (QBIS-CAT), Institut de Química Computacional i Catálisi (IQCC), Departament de Química, Universitat de Girona, C/M. Aurèlia Capmany 69, 17003 Girona, Catalonia, Spain
[§]Department of Chemistry and Center for Metals in Biocatalysis, University of Minnesota, 207 Pleasant Street SE, Minneapolis, Minnesota 55455, United States
[∥]Institute of Chemical Research of Catalonia (ICIQ), The Barcelona Institute of Science and Technology, Avinguda Països Catalans 16, 43007 Tarragona, Spain
[⊥]Grup de Química Supramolecular, Institut de Ciència Molecular, Departament de Química Inorgànica, Universitat de València, 46980 Paterna, Valencia, Spain

Supporting Information

ABSTRACT: The reaction of $[(PyNMe_3)Fe^{II}(CF_3SO_3)_2]$, **1**, with excess peracetic acid at −40 °C generates a highly reactive intermediate, **2b**(PAA), that has the fastest rate to date for oxidizing cyclohexane by a nonheme iron species. It exhibits an intense 490 nm chromophore associated with an $S = 1/2$ EPR signal having g-values at 2.07, 2.01, and 1.94. This species was shown to be in a fast equilibrium with a second $S = 1/2$ species, **2a**(PAA), assigned to a low-spin acylperoxoiron(III) center. Unfortunately, contaminants accompanying the **2**(PAA) samples prevented determination of the iron oxidation state by Mössbauer spectroscopy. Use of MeO-$PyNMe_3$ (an electron-enriched version of $PyNMe_3$) and cyclohexyl peroxycarboxylic acid as oxidant affords intermediate **3b**(CPCA) with a Mössbauer isomer shift $\delta = -0.08$ mm/s that indicates an iron(V) oxidation state. Analysis of the Mössbauer and EPR spectra, combined with DFT studies, demonstrates that the electronic ground state of **3b**(CPCA) is best described as a quantum mechanical mixture of $[(MeO\text{-}PyNMe_3)Fe^{V}(O)(OC(O)R)]^{2+}$ (~75%) with some $Fe^{IV}(O)(^{\bullet}OC(O)R)$ and $Fe^{III}(OOC(O)R)$ character. DFT studies of **3b**(CPCA) reveal that the unbound oxygen of the carboxylate ligand, O2, is only 2.04 Å away from the oxo group, O1, corresponding to a Wiberg bond order for the O1–O2 bond of 0.35. This unusual geometry facilitates reversible O1–O2 bond formation and cleavage and accounts for the high reactivity of the intermediate when compared to the rates of hydrogen atom transfer and oxygen atom transfer reactions of $Fe^{III}(OC(O)R)$ ferric acyl peroxides and $Fe^{IV}(O)$ complexes. The interaction of O2 with O1 leads to a significant downshift of the Fe–O1 Raman frequency (815 cm^{-1}) relative to the 903 cm^{-1} value predicted for the hypothetical $[(MeO\text{-}PyNMe_3)Fe^{V}(O)(NCMe)]^{3+}$ complex.

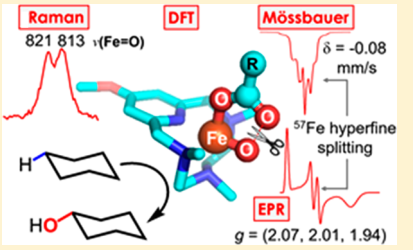

INTRODUCTION

High-valent oxoiron species are nature's tool for functionalizing inert molecules such as aliphatic C–H bonds.[1−6] Oxoiron(IV) species have been identified as the C–H cleaving agents in several mono- and dinuclear nonheme iron enzymes.[7−9] Parallel efforts with oxoiron(IV) synthetic models of these enzymes have shown that they can break strong C–H bonds, although at reaction rates that still fall short when compared with enzymatic systems.[10−13] Higher oxidation states are accessed in many cytochrome P450s and peroxidases via a species known as compound I that is best described as an oxoiron(IV)–porphyrin cation radical.[14] Oxoiron(V) species have been proposed as the reactive intermediate in the catalytic cycle of Rieske oxygenase enzymes,[15−17] although direct detection of this species has not been reported. Synthetic nonheme oxoiron(V) compounds are rare (Scheme 1). Tetraamido macrocyclic ligands (TAML) have for the first time allowed the stabilization, spectroscopic characterization, and reactivity analysis of an oxoiron(V) species,[18−23] and only recently has an oxoiron(V) imido complex been described.[24] $[(L)Fe^{V}(O)(R)]$ (L = neutral polyamine ligand, R = OH or O_2CR) species have been proposed to be reactive intermediates in the oxidation of hydrocarbons.[25−28] Their implication in

Received: October 31, 2017
Published: February 20, 2018

DOI: 10.1021/jacs.7b11400
J. Am. Chem. Soc. XXXX, XXX, XXX−XXX

Scheme 1. Spectroscopically Characterized Oxoiron(V) Complexes

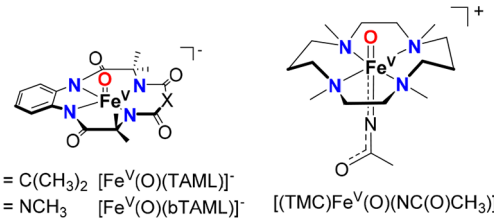

these reactions has been deduced based on indirect evidence such as product analyses with substrate probes and isotope labeling and by computational methods.[29−31] In addition, such oxoiron(V) species have been detected in trace quantities by cryospray mass-spectrometry[32−34] or by EPR,[34−36] but no definitive characterization has been reported. In some instances, claimed Fe^{V} species have been shown[37] or reinterpreted to be ferric species.[37,38]

Putative $[(L)Fe^{V}(O)(O_2CR)]^{2+}$ intermediates (where L stands for a neutral tetradentate aminopyridine ligand) are of interest because there is mounting evidence that they perform the stereoretentive hydroxylation of aliphatic C−H bonds, a distinctively difficult but powerful reaction in organic synthesis and biology.[39,40] Stereospecific hydroxylation entails two difficult steps. The first is the breakage of a strong C−H bond, usually considered inert toward common organic reagents, via a fast hydrogen atom transfer reaction, creating a carbon-centered radical. In a second step, this extremely short-lived radical reacts with the hydroxyl ligand, avoiding escape into the solvent.[41,42]

We have recently described the generation of a highly reactive $S = 1/2$ species (called **2b** by Serrano-Plana et al.[43]) from the reaction of $[(PyNMe_3)Fe^{II}(CF_3SO_3)_2]$, **1**, with peracetic acid (PAA) at cryogenic temperatures (Scheme 2).[43,44] Species **2b** has *g*-values at 2.07, 2.01, and 1.94 that are difficult to reconcile with a low-spin ferric assignment; spectral simulation of the signal showed that it accumulated to approximately 40% of the iron in the sample. EPR also indicated that this species is in fast equilibrium with $S = 1/2$ species **2a** (~5% of the Fe). On the basis of its *g*-values at 2.20, 2.19, and 1.99, species **2a** was assigned as $[(PyNMe_3)Fe^{III}(\kappa^2\text{-}OOAc)]^{2+}$. Product analysis, EPR, and mass spectrometry experiments initially led us to formulate **2b** as $[(PyNMe_3)Fe^{V}(O)(OAc)]^{2+}$. The Fe(V) species described in this work differs from those with tetraanionic tetraamido ligands such as TAML in having a neutral supporting ligand, which leads to the observation of extraordinary oxidation reactivity. Compound **2b** oxidizes hydrocarbons at a record fast rate among synthetic nonheme iron systems and reproduces the reactivity of P450 compound I in terms of reaction rates and stereospecificity. Because of the presence of at least six other paramagnetic species in the reaction mixture, the Mössbauer spectra of **2b**, crucial for the assignment of its oxidation state, could not be identified.

Scheme 2. Proposed Intermediates Formed in the Reactions of 1 and 1′ with Various Peracids (PAA = Peracetic Acid, CPCA = Cyclohexyl Peroxyacid, PNA = Pernonanoic Acid

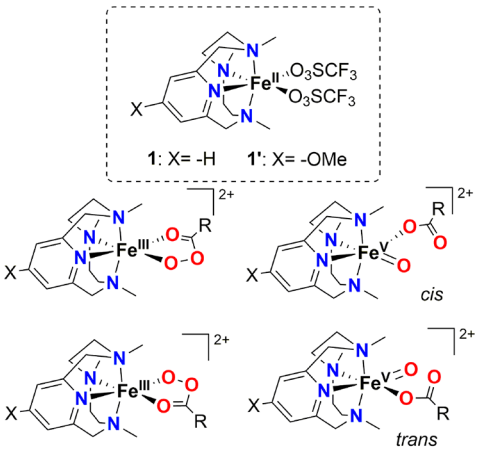

X	R	Fe^{III}	Fe^{V}
H	CH_3	**2a(PAA)**	**2b(PAA)**
H	cyclohexyl	**2a(CPCA)**	**2b(CPCA)**
H	$CH_3(CH_2)_7$	**2a(PNA)**	**2b(PNA)**
OMe	CH_3	**3a(PAA)**	**3b(PAA)**
OMe	cyclohexyl	**3a(CPCA)**	**3b(CPCA)**
OMe	$CH_3(CH_2)_7$	**3a(PNA)**	**3b(PNA)**

Herein, we describe critical improvements that have enabled a full spectroscopic and computational characterization of the complex of interest. By replacing the $PyNMe_3$ ligand with the electron-enriched version MeO-$PyNMe_3$ and using cyclohexyl peroxycarboxylic acid (CPCA) as the oxidant, we were able to generate the corresponding species in nearly 50% yield. Our combined spectroscopic and DFT analysis suggests an unprecedented electronic structure for a high-valent iron complex, which in turn provides insight into its unique reactivity.

RESULTS

The spectral properties of the intermediate of interest depend on the combination of ligand/oxidant (Table 1). Below we use the following designations: **2** for $PyNMe_3$ and **3** for MeO-$PyNMe_3$ complexes. The oxidant used is indicated in parentheses, e.g., **2**(PAA), **3**(CPCA), **3**(PNA), etc. The UV−vis absorption spectrum of **3**(CPCA) shown in Figure 1 shows two principal absorption features in the visible region, a more intense feature with λ_{max} = 520 nm and a weaker band near 700 nm. These features are blue-shifted in **2**(CPCA) upon changing the supporting ligand from MeO-$PyNMe_3$ to $PyNMe_3$ (Table 1). Comparison among complexes in the **3** series shows that the nature of the R group on the peracid also affects the observed absorption maxima slightly.

EPR Results. Intermediates **2** and **3** exhibit $S = 1/2$ EPR signals that represent two subspecies **a** and **b**, which are present in different ratios depending on the supporting ligand and are involved in a fast equilibrium (Table 1). Subspecies **a** has a low-spin Fe^{III} center, whereas **b**, as shown below, is predominantly Fe^{V}. The main text focuses on **3b**(CPCA), while corresponding results for **2b**(CPCA) are presented in the SI. The subspecies of **2**(PAA), **2**(CPCA), and **2**(PNA) occur in the ratio [**b**]/[**a**] ≈ 8−10:1, while subspecies **a** is almost absent (<2% of total Fe) in **3**(CPCA). Figure 2 shows X-band spectra of **3**(CPCA) containing ^{57}Fe in natural abundance (2.2%, panel A) and enriched to 95% (panel B). Unenriched **3**(CPCA) exhibits an $S = 1/2$ EPR signal with *g*-values at 2.07, 2.01, and 1.94, the same *g*-values as reported for **2b**(PAA).[43] This signal is thus associated with **3b**(CPCA). The low-spin Fe^{III} species **3a**(CPCA) was essentially absent in the sample; i.e., by spectral simulations we found [**3b**(CPCA)]/[**3a**(CPCA)] ≈ 50:1, which greatly simplifies the Mössbauer analysis as the features of **3a**(CPCA) represent only 1% of the iron in the Mössbauer

DOI: 10.1021/jacs.7b11400
J. Am. Chem. Soc. XXXX, XXX, XXX−XXX

Table 1. Comparison of Some Spectroscopic Properties of Complexes 2 and 3

Samples	UV−vis data λ_{max} (nm)	Raman data (cm^{-1})[a] (815/829 intensity ratio) [^{18}O-PNA data]	g = 2.07/g = 2.7 signal intensity ratio
2(PAA)	490, 680	815/829 (8:1)(exc 561 nm)	8:1 (EPR)[43]
2(CPCA)	504, 685	815/829 (8:1) (exc 561 nm)	11:1 (EPR) 7:1 (Mössbauer)
2(PNA)	496, 685	815 [783][c]/829 [?][b] (11:1) (exc 515 nm)	9:1 (EPR) 10:1 (Mössbauer)
3(PAA)	508, 683	812/820 Fermi doublet 829 not obsvd (exc 515 nm)	N/A
3(CPCA)	520, 700	812/820 Fermi doublet 829 not obsvd (exc 515 nm)	50:1 (EPR)
3(PNA)	512, 685	813/821 Fermi doublet [784][b] 829 not obsvd (exc 515 nm)	40:1 (EPR)

[a]Entries in square brackets correspond to data obtained with ^{18}O-PNA. [b]While the 771 cm^{-1} peak is observed in the spectra of **2**(^{18}O-PNA) and **3**(^{18}O-PNA), the 829 cm^{-1} peak is not observed in **3**(^{16}O-PNA). Therefore, it cannot be connected to the 829 cm^{-1} peak.

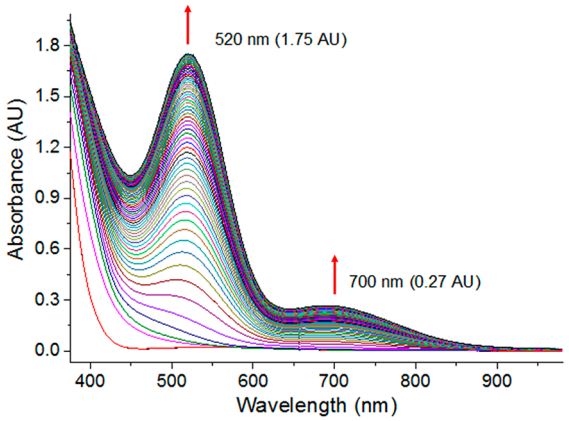

Figure 1. UV−vis spectra of $[(MeO\text{-}PyNMe_3)Fe^{V}(O)(OC(O)cy)]^{2+}$, **3**(CPCA), in 3:1 acetone/MeCN in a 1 cm cuvette. Solid lines show progressive formation of **3**(CPCA) upon addition of 10 equiv of CPCA to 0.5 mM $[(MeO\text{-}PyNMe_3)Fe^{II}(CF_3SO_3)_2]$ at −60 °C. $\varepsilon(\lambda_{max}$ = 520 nm) ≈ 7500 M^{-1} cm^{-1}. The bands at 520 and 700 nm increase monotonically over 200 s upon addition of CPCA.

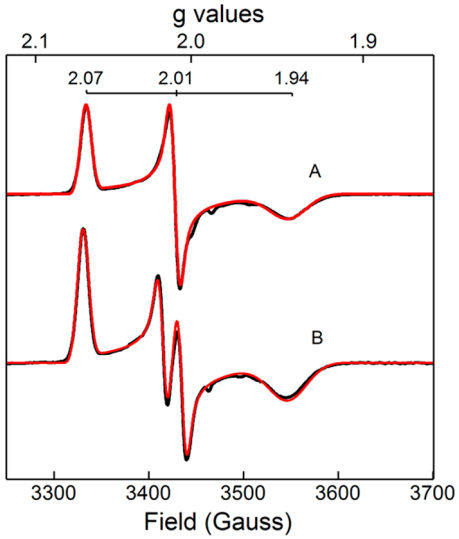

Figure 2. X-band EPR spectra of **3b**(CPCA) recorded at T = 15 K. Samples were prepared by adding 10 equiv of CPCA to a 1 mM solution of $[(MeO\text{-}PyNMe_3)Fe^{II}(CF_3SO_3)_2]$ at −70 °C. (A) ^{57}Fe in natural abundance (2.2%); full scan and low field region are shown in Figures S19 and S20. (B) Spectrum of **3b**(CPCA) 95% enriched with ^{57}Fe. The red lines are SpinCount simulations for g_x = 2.010, g_y = 2.067, g_z = 1.941. For the line shapes it was assumed that the g-values have a Gaussian distribution with $\sigma(g_x)$ = 0.00, $\sigma(g_y)$ = 0.002, and $\sigma(g_z)$ = 0.010; 0.45 mT packet width. The spectrum of the enriched sample was simulated with the same g-values and line width parameters, adding a ^{57}Fe magnetic hyperfine interaction term. The results are listed in Table 2. Instrumental conditions: (A) 0.2 mW, (B) 0.002 mW, microwave power (change of microwave power is accidental, not dictated by saturation considerations); 0.3 mT, modulation amplitude for both.

spectrum (the Mössbauer spectrum of **2a**(CPCA) is hidden under the features of **2b**(CPCA); see section III of the SI). Importantly, samples of **3b**(CPCA) were free of other S = 1/2 species but contained various high-spin Fe^{III} species (EPR spectra are shown in Figures S19−22).

The spectra of **3b**(CPCA) are described with the S = 1/2 spin Hamiltonian

$$\hat{H} = \beta\hat{\mathbf{S}}\mathbf{g}\mathbf{B} + \hat{\mathbf{S}}\mathbf{A}\hat{\mathbf{I}} + \hat{H}_Q + \hat{H}_Z \quad (1)$$

$$\hat{H}_Q = \frac{eQV_{zz}}{12}\left[3\hat{I}_z^2 - \frac{15}{4} + \eta(\hat{I}_x^2 - \hat{I}_y^2)\right] \quad (1a)$$

$$\hat{H}_Z = -g_n\beta_n\mathbf{B}\hat{\mathbf{I}} \quad (1b)$$

where **A** is the ^{57}Fe magnetic hyperfine tensor, $\hat{H}_Z$ describes the ^{57}Fe nuclear Zeeman interaction, and $\hat{H}_Q$ describes the interaction of the electric field gradient (EFG) tensor with the ^{57}Fe nuclear quadrupole moment, Q, of the nuclear excited state; $\eta = (V_{xx} - V_{yy})/V_{zz}$ is the asymmetry parameter. The x axis was chosen to be along $g_{mid} = g_x$ = 2.01; this choice will be convenient for the presentation of the DFT results and for comparison with published data of Fe^{IV}=O complexes for which the z axis is generally chosen to be along the Fe=O bond. Because **g** is nearly isotropic the Mössbauer data do not convey information about the orientations of the **A**- and EFG-tensors relative to **g**, and we thus assumed that **g** and **A** are collinear for the simulations of the Mössbauer spectra. The line widths (fwhm) of the g_x = 2.01 and g_y = 2.07 features are about 1.7 mT, while the width of the g_z = 1.94 feature is 4.3 mT. Most probably, the broadening of the g_z feature results from a conformational heterogeneity that affects, for reasons presently not understood, essentially g_z. DFT calculations, described below, show that unresolved ^{14}N hyperfine interactions of the four nitrogen donors of $MeO\text{-}PyNMe_3$ are too small to be responsible for the broadening.

When **3b**(CPCA) is enriched with ^{57}Fe its g_{mid} = 2.01 feature is split into a doublet corresponding to $|A_{g=2.01}|$ = 57 MHz. The 57-MHz value seemed to be somewhat at odds with the Mössbauer analysis which yielded $A_{x'}$ = −62 MHz (see below), but the differences could be reconciled by allowing that $A_{g=2.01}$ extracted from EPR is not a principal axis value. By assuming that the **g** and **A** tensors have a common z-axis and allowing a rotation of 20° around z, the splitting at $g_{mid} = g_{x'}$ could be simulated for A_x = 62 MHz. Approximately consistent with this result, the DFT solution presented below yields α = 26°. Our simulations suggest that the signals at the other two g values

DOI: 10.1021/jacs.7b11400
J. Am. Chem. Soc. XXXX, XXX, XXX−XXX

have much smaller A-values ($A_y \approx -8(4)$ MHz and $A_z \approx -9(3)$ MHz, with the signs determined from the Mössbauer analysis). The $S = 1/2$ center of **3b**(CPCA) thus exhibits quite a large **A** tensor anisotropy. As expected, the g_{mid} splitting can be simulated as well by rotating **A** by 30° around y.

Our aim is to determine the nature and the Fe oxidation state of **3b**(CPCA). As considered for other κ^2-acylperoxoiron(III) intermediates proposed for bioinspired iron catalysts,[37,45] the obvious candidates are the three isoelectronic $S = 1/2$ states $[(\text{MeO-PyNMe}_3)\text{Fe}^{\text{III}}(\kappa^2\text{-OOC(O)cy})]^{2+}$, $[(\text{MeO-PyNMe}_3)\text{Fe}^{\text{IV}}(\text{O})(^{\bullet}\text{OC(O)cy})]^{2+}$ and $[(\text{MeO-PyNMe}_3)\text{Fe}^{\text{V}}(\text{O})\text{-(OC(O)cy)}]^{2+}$. Of these three options, the proposed Fe^{IV}═O/carboxyl radical species would be inconsistent with the observed **A** tensor anisotropy observed by EPR and Mössbauer spectroscopy (see below) as an axial **A** tensor with two large components and one small one (along the Fe−O bond) would be expected for the $d_{xy}^2 d_{xz}^1 d_{yz}^1$ configuration of the Fe^{IV}═O unit, as observed for all $S = 1$ Fe^{IV}═O complexes reported thus far.[46,47] On the other hand, an Fe^{V}═O complex would exhibit an **A** tensor with only one large (along x if the α-HOMO is d_{yz}) and two small components (y and z), reflecting an electronic structure with one unpaired electron in one of the d-orbitals, as reported and analyzed for $[(\text{TAML})\text{Fe}^{\text{V}}(\text{O})]^-$ and $[(\text{TMC})\text{-(O)Fe}^{\text{V}}(\text{NR})]^+$.[18,24]

By obtaining UV−vis spectra of **3b**(CPCA) solutions and quantifying the spin concentrations of the same samples, the extinction coefficient ε_{520} of **3b**(CPCA) can be determined. For two samples of **3b**(CPCA) containing 0.5 mM Fe (UV−vis spectrum shown in Figure 1), we obtained 0.223 and 0.245 mM spins. Based on the average of 0.234 mM, we conclude that **3b**(CPCA) in these samples represents 47% of the iron in the sample, in excellent agreement with the Mössbauer result (48%, see Figure 3), with an ε_{520} value ~7500 $M^{-1}cm^{-1}$. The uncertainties for the quoted ε are estimated to be ±15%. Note that we reported an ε_{490} of ~4500 $M^{-1}cm^{-1}$ for **2b**(PAA),[43] a value that we have confirmed in this study, suggesting that the introduction of a 4-methoxy substituent on the pyridine of the supporting ligand of **3b**(CPCA) can result in a higher extinction coefficient. The implications of this observation will be discussed in a later section.

Mössbauer Studies. Figure 3A shows a 4.2 K Mössbauer spectrum of a sample containing **3b**(CPCA). The spectrum was recorded in a parallel field of $B = 7.0$ T; spectra recorded for $B = 2.0$ and 4.0 T are shown in Figure 4. The feature outlined in magenta represents high-spin ($S = 5/2$) Fe^{III} contaminants (at least four species) accounting for ca. 42% of the Fe in the sample. X-band EPR (see section II of the SI) revealed a major component with $D \approx 0.7$ cm^{-1} and $E/D \approx 0.16$ representing about 70% of the high-spin (HS) Fe^{III}; D and E/D are the commonly used zero-field splitting parameters. The SI describes our understanding of the HS ferric components (in particular see Table S4). A 7.0-T Mössbauer spectrum of a decayed sample of **2b**(PNA) showing mainly HS ferric components is also included (Figure S45).

In the Mössbauer spectra of Figures 3 and 4, species **3b**(CPCA) absorbs in the velocity range -3 mm/s $< v <$ +2.5 mm/s. This range contains two contaminant lines from the high-spin Fe^{III} species (magenta curve in Figure 3A). Because the D values are small, the $B = 7.0$ T spectra of the Fe^{III} components are independent of D and E/D. Importantly, the intensities and positions of the two contaminant lines in question are known once the positions and shapes of the outer lines are determined. The outermost lines in Figure 3A result

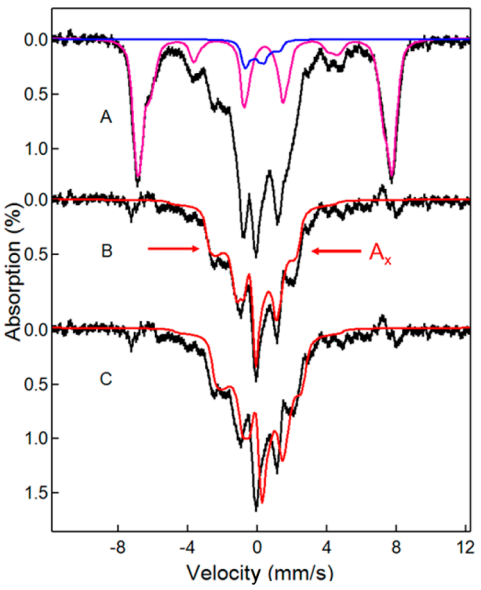

Figure 3. (A) Mössbauer spectrum of **3b**(CPCA) obtained at 4.2 K for $B = 7.0$ T, applied parallel to the observed γ rays (^{57}Fe concentration 1 mM). The magenta curve represents a spectral simulation for the HS Fe^{III} contaminants (42% of Fe). The blue curve outlines 5% of an indicated $[(\text{MeO-PyNMe}_3)\text{Fe}^{\text{IV}}(\text{O})]^{2+}$ contaminant. (B) Spectrum of **3b**(CPCA), in black, obtained by subtracting the magenta and blue curves from the black line shown in the top spectrum. The red line (drawn to represent 48% of total Fe) is a spectral simulation for **3b**(CPCA) for $\delta = -0.08$ mm/s. The horizontal arrows mark the splitting due to A_x. (C) Theoretical curve for **3b**(CPCA) assuming a $\delta = 0.26$ mm/s pertinent for a low-spin ferric $[(\text{MeO-PyNMe}_3)\text{Fe}^{\text{III}}(\text{OOR})]^{2+}$ species. We estimate that the sample contains 45−50% of species **3b**(CPCA). This percentage agrees well with the EPR result and the fraction of **2b**(CPCA) generated by reaction of $[(\text{PyNMe}_3)\text{Fe}^{\text{II}}(\text{CF}_3\text{SO}_3)_2]$ with CPCA described in section III of the SI.

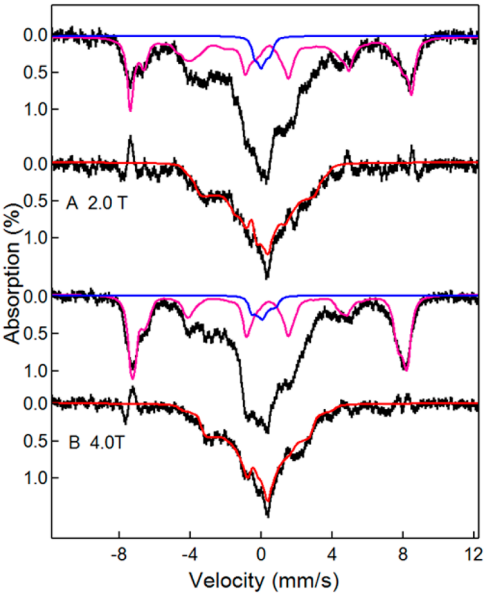

Figure 4. 4.2 K spectra of **3b**(CPCA) recorded in applied fields of $B =$ 2.0 T (A) and 4.0 T (B). The magenta and blue lines indicate, respectively, Fe^{III} and Fe^{IV} contaminants mentioned in the caption of Figure 3.

DOI: 10.1021/jacs.7b11400
J. Am. Chem. Soc. XXXX, XXX, XXX−XXX

Table 2. Spin Hamiltonian Parameters for $[(MeO\text{-}PyNMe_3)Fe^{V}(O)(OC(O)cy)]^{2+}$ (**3b**(CPCA)), $[(PyNMe_3)Fe^{V}(O)(OC(O)cy)]^{2+}$ (**2b**(CPCA)), and Related Complexes[a]

complex	$g(x,y,z)$	$A(x,y,z)$ (MHz)[b]	ΔE_Q (mm/s)	η	δ (mm/s)
3b(CPCA)	2.01, 2.07, 1.94	−62(2), −8(4), −9(3)	+1.15(30)	0.6	−0.08(3)
	2.02, 2.04, 1.99	*−56, −18, −5*	*+0.78*	0.3	*-0.01*
2b(CPCA)	2.01, 2.07, 1.94	−62(2), −7(4), −10(4)	+1.00(30)	0.2	−0.06(3)
	2.02, 2.04, 1.99	*−57, −18, −5*	*+0.86*	0.3	*-0.01*
2b(PNA)	2.01, 2.07, 1.94	−62(2), −6(4), −11(4)	+1.11(25)	0.3	−0.08(3)
$[(TAML)Fe^{V}(O)]^{-}$[c,d]	1.99, 1.97, 1.74	−67.5(14), −2.0(20), −22.3(21)	4.25(10)	0.65(10)	−0.42(3)
		−59.8, −13.0, −20.6	4.51	0.72	*-0.39*
$[(TMC)Fe^{V}(O)\text{-}(NC(OH)CH_3)]^{2+}$[e]	2.05, 2.01, 1.97	−47(2), −17(2), 0(5)	−0.2	−3	+0.10
	2.03, 2.00, 1.97	*−45, −14, −6*			

[a]Values predicted by DFT are shown in italics. [b]Numbers in parentheses are estimated uncertainties in the least significant digits. [c]Reported by Tiago de Oliveira et al.[18] [d]Table 1 of van Heuvelen et al.[18] listed the A-values of $[(TAML)FeV(O)]^{-}$ erroneously in units of tesla ($A/g_n\beta_n$), as originally reported,[18] rather than MHz as stated. [e]The parameters of $[(TMC)FeV(O)(NC(OH)CH_3)]^{2+}$ are different from the other three complexes in this table due to the strong trans effect of the imido ligand on the Fe=O bond.[24]

from $M_S = -5/2$ levels; the weak features near −3 mm/s and +5 mm/s belong to $M_S = -3/2$ states which are populated at 4.2 K by ∼8%. We have fitted the outermost features of the high-spin Fe^{III} species with various assumptions and found that the position and intensity of the inner two lines are essentially independent of these assumptions. Thus, by subtracting the simulated high-spin Fe^{III} components (Table S4, SI) from the raw data we obtain quite reasonable representations of **3b**(CPCA). By comparing various preparations of **2b**(PAA) and **3b**(CPCA), and creating difference spectra, we deduced that ∼5% of the Fe of the sample of Figure 3A belongs to $[(MeO\text{-}PyNMe_3)Fe^{IV}(O)(MeCN)]^{2+}$; this Fe^{IV} species (we have spectra of this species for $PyNMe_3$; see SI, Figure S26) contributes a quadrupole doublet for $B < 0.1$ T (the blue line in Figure 3A represents a $B = 7$ T simulation of this contaminant.). Figure 3B, then, shows the desired 7.0 T spectrum of **3b**(CPCA).

A comment about the quadrupole splitting, ΔE_Q, and the isomer shift, δ, of **3b**(CPCA) is in order. If at higher temperatures, say 150 K, the relaxation of the electronic spin would be fast compared to the nuclear precession frequencies, **3b**(CPCA) would exhibit a quadrupole doublet from which ΔE_Q and δ could readily be extracted. However, the relaxation rate of **3b**(CPCA) is still too slow at 150 K. Attempts to increase this rate by inducing spin−spin relaxation using a 5 mM Fe concentration sample failed. Thus, δ, the most important parameter for determining the oxidation state of **3b**(CPCA), has to be extracted by simulating the paramagnetic hyperfine structure of the 4.2 K spectra. We have previously described a similar situation for $[(TMC)Fe^{V}(O)(NC(O)\text{-}CH_3)]^{+}$ and its conjugate acid $[(TMC)Fe^{V}(O)(NC(OH)\text{-}CH_3)]^{2+}$.[24]

The principal features of the Mössbauer spectra are readily understood by taking into account the EPR information that the ^{57}Fe **A** tensor of **3b**(CPCA) has one large component (along x) and two small ones and that the g-values are nearly isotropic. The largest magnetic splitting, indicated in Figure 3B by the horizontal arrows (the "base"), reflects molecular orientations in the frozen solution sample for which the applied magnetic field is near the axis of A_x; our simulations suggest that $A_x \approx -62 \pm 2$ MHz (Note: $A_x = -62$ MHz corresponds to $A_x/g_n\beta_n = -45.3$ T, the quantity most often quoted in the Mössbauer literature). This value yields an effective magnetic field $B_{eff} = B_{int} + B = (-(1/2) \times 45.3 + 7.0)$ T $= -15.7$ T at the ^{57}Fe nucleus. Simulations of the inner "triplet" feature yielded $A_y \approx -8(4)$ MHz and $A_z \approx -9(3)$ MHz, i.e., components with values that are substantially smaller than that of A_x, consistent with the EPR results.

The component of the EFG tensor along A_x is negative, while those along y and z are positive. These sign choices shift the "base" to more negative and the "triplet" to more positive Doppler velocities. Our simulations, as well as least-squares group fits to the 2.0, 4.0, and 7.0 T spectra, suggest that $\Delta E_Q \approx +1.15$ mm/s and $\eta \approx 0.6$. We have also recorded spectra for $B = 45$ mT applied parallel as well as perpendicular to the γ-rays. At $T = 4.2$ K and $B = 45$ mT, the Fe^{III} contaminants contribute as many as 12 Mössbauer spectra, one for each Kramers doublet of the four identified species. These spectra depend, for each contaminant, on D, E/D, the **A** tensor, ΔE_Q, and parameters describing the distribution of the zero-field splitting parameters. Moreover, for $D \approx 0.7$ cm^{-1} the middle Kramers doublets are ∼35% populated at 4.2 K and would produce spectra entirely hidden under the absorption of **3b**(CPCA). The 45 mT spectra were insufficiently resolved to be useful. The spin Hamiltonian parameters of **3b**(CPCA) that give the simulated spectrum in Figure 3B are listed in Table 2. The parameters extracted for **2b**(CPCA) are essentially the same as those of **3b**(CPCA); spectra of **2b**(CPCA) obtained at $B = 7.0$ and 4.0 T are shown in Figures S24 and S25, respectively.

The isomer shift, $\delta = -0.08 \pm 0.03$ mm/s, of **3b**(CPCA) was obtained by group fitting the 2.0, 4.0, and 7.0 T spectra. The value of δ obtained is substantially more negative than the value of $\delta = +0.05$ mm/s found for $[(PyNMe_3)Fe^{IV}(O)(MeCN)]^{2+}$, **4** (see section IV of the SI), demonstrating that **3b**(CPCA) must represent a species in a higher oxidation state than **4**. Also, **3b**(CPCA) cannot be assigned to an Fe^{III}−peroxo species such as $[(MeO\text{-}PyNMe_3)Fe^{III}(\kappa^2\text{-}OOCR)]^{2+}$ for which we obtained a δ value of +0.26 mm/s by DFT. For illustration, Figure 3C shows a simulation for $\delta = +0.26$ mm/s, a value clearly inconsistent with the data. These arguments suggest the assignment of **3b**(CPCA) as $[(MeO\text{-}PyNMe_3)Fe^{V}(O)(OC\text{-}(O)cy)]^{2+}$, resulting from O−O bond heterolysis of an initially formed but unobserved $[(MeO\text{-}PyNMe_3)Fe^{III}(\kappa^2\text{-}OOCR)]^{2+}$ precursor (for the $PyNMe_3$ ligand, this precursor is the $g_{max} = 2.20$ species, **2a**(PAA)). We have assigned here a pure oxidation state to the iron in **3b**(CPCA). Such an assignment is perfectly appropriate for $[(TAML)Fe^{V}(O)]^{-}$, which by all measures is a pure $S = 1/2$ Fe^{V}−oxo complex, as the tetraanionic TAML ligand stabilizes the Fe^{V} oxidation state. Complexes with neutral supporting ligands such as MeO-

DOI: 10.1021/jacs.7b11400
J. Am. Chem. Soc. XXXX, XXX, XXX−XXX

PyNMe$_3$ and TMC, respectively, found in **3b**(CPCA) and [(TMC)Fe^{V}(O)(NC(OH)CH$_3$)]$^{2+}$ (see Figure 5 of the work

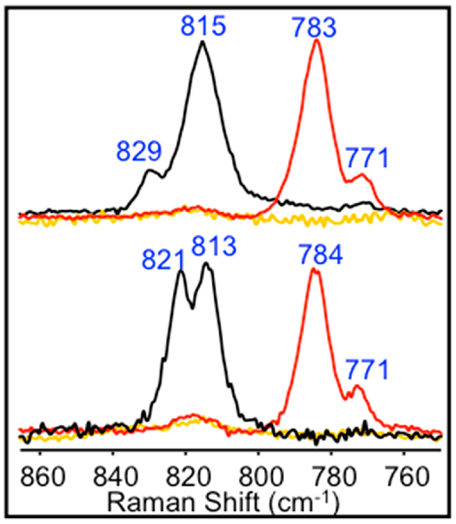

Figure 5. Resonance Raman spectra in CH_3CN/CD_3COCD_3 (v/v 1:3). Top: **2**(PNA) (2 mM Fe) (λ_{ex} = 515 nm) (black, using ^{16}O-PNA, red, using ^{18}O-PNA, and orange, decayed. Bottom: **3**(PNA) (2 mM Fe) (λ_{ex} = 515 nm) (black, using ^{16}O-PNA, red, using ^{18}O-PNA), and orange, decayed). All spectra were collected at 77 K. See Figure S32 for corresponding spectra using PAA and CPCA.

by Van Heuvelen et al.[24]) would have electronic configurations with some Fe^{IV}/radical character due to the greater electrophilicity of the high-valent metal centers in these complexes. We return to this point in the section describing the DFT results.

The obtained *A*-values also exclude the possibility that **3b**(CPCA) is a complex comprising an S = 1 Fe^{IV}=O complex antiferromagnetically coupled to a carboxyl radical. Typical (local) *a*-values (in $\boldsymbol{S}\boldsymbol{a}^{S=1}\boldsymbol{I}$, S = 1) for S = 1 Fe^{IV}=O complexes are $a_x \approx a_y = -(25-29)$ MHz and $a_z \approx -7$ MHz. When referred to the spin Hamiltonian of an antiferromagnetically coupled Fe^{IV}=O/radical state, these *a*-values would change to $A_x \approx A_y = -(33-44)$ MHz and $A_z \approx -9$ MHz (in $\boldsymbol{S}\boldsymbol{A}^{S=1/2}\boldsymbol{I}$, S = 1/2); the two tensors are related by $\boldsymbol{A}^{S=1/2} = (4/3)\,\boldsymbol{a}^{S=1}$, where 4/3 is a spin projection factor. For the S = 1 heme/porphyrin radical complex of horseradish peroxidase, HRP I, Debrunner and co-workers[48] reported a Mössbauer analysis with $a_x = a_y = -26.5$ MHz, while an ENDOR study by Hoffman et al.[49] gave $A_x = A_y = -35$ MHz (thus a_x/A_x near 4/3). To conclude, the Mössbauer data of **3b**(CPCA) show that the observed **A** tensor and the value of δ are not compatible with its assignment to an Fe^{IV}–oxo radical species.

The values for A_x obtained from the EPR and Mössbauer analysis are quite accurate. Although A_y and A_z have larger uncertainties, reasonable simulations can be obtained by simultaneously increasing A_y and decreasing A_z while keeping $(A_y + A_z)/2$ near −9 MHz. We estimate that ΔE_Q is accurate within ±0.3 mm/s; in the simulations this parameter is strongly correlated with the asymmetry parameter η, as both determine the component of the EFG along A_x.

Resonance Raman and XAS Studies. To provide additional insight into the nature of **2b**(CPCA) and **3b**(CPCA), further spectroscopic studies were carried out on these intermediates and related complexes (Scheme 2). Resonance Raman spectra were obtained for samples prepared by reacting the Fe^{II} precursor in a (v/v 1:3) CH_3CN/CD_3COCD_3 solution with 5–10 equiv of peracid at −65 °C. Similar spectra were obtained for the three different peracids used in this study (Table 1). Of particular use was pernonanoic acid (PNA), for which a method was available for the synthesis of the ^{18}O-labeled peracid (see section XII in the SI). **2**(PNA) exhibits two resonantly enhanced Raman bands at 815 and 829 cm^{-1} in an 11:1 intensity ratio (Figure 5 top, black trace), which disappear, together with the UV–vis chromophore, upon warming up the sample to room temperature. These two features are also observed in the resonance Raman spectra of **2**(PAA) and **2**(CPCA) with a comparable intensity ratio (Table 1 and Figure S32). With ^{18}O-labeled PNA, the 815 cm^{-1} band downshifted to 783 cm^{-1} (Figure 5 top, red trace), corresponding to a 32 cm^{-1} decrease that is consistent with its assignment to a ν(Fe=O) mode based on a Hooke's Law calculation for a diatomic Fe=O bond. On the other hand, **3**(PNA) exhibits a pair of peaks at 813 and 821 cm^{-1} (Figure 5 bottom, black trace), which collapse into one peak at 784 cm^{-1} with ^{18}O-labeled PNA (Figure 5 bottom, red trace). Given that both ^{18}O-labeled intermediates exhibit essentially one vibration at the same frequency, the pair of peaks observed in **3**(^{16}O-PNA) represent a Fermi doublet with a frequency centered at 817 cm^{-1} that is assigned to the ν(Fe=O) mode of **3b**. These two 800 cm^{-1} features with near equal intensities are also observed in the resonance Raman spectra of **3b**(PAA) and **3b**(CPCA) (Figure S32).

The 829 cm^{-1} peak observed in the resonance Raman spectra of samples of **2**, but not of **3**, belongs to a different species. Designated as **2a**, it exhibits ∼10% of the intensity of the corresponding 815 cm^{-1} peak in samples of **2**(PAA), **2**(CPCA) and **2**(PNA) that is assigned to **2b**. The use of ^{18}O-labeled PNA results in the disappearance of the 829 cm^{-1} peak. If this peak were to arise from an Fe=O unit, it would be expected based on Hooke's Law to shift to ∼795 cm^{-1} but such a shifted feature is not observed at this frequency. On the other hand, it could arise from **2a**, the acylperoxoiron(III) isomer of **2b** and be assigned as its O–O stretch. Such a mode would have a Hooke's Law-calculated downshift of ∼47 cm^{-1} and a predicted peak position of 782 cm^{-1}, which unfortunately would be obscured by the dominant peak at 783 cm^{-1} arising from ^{18}O-labeled **2b** (Figure 5).

Scrutiny of the 783 cm^{-1} region does reveal a shoulder at 771 cm^{-1} with about 15% the intensity of the 783 cm^{-1} band. The 771 cm^{-1} band is not observed in the spectra of the ^{16}O-isotopomers but is also observed in the spectrum of **3**(^{18}O-PNA), even though the spectrum of **3**(^{16}O-PNA) does not exhibit a peak at 829 cm^{-1}, so the 771 cm^{-1} feature cannot be associated with the 829 cm^{-1} peak. It is however resonance-enhanced because it is absent in the decayed samples. The band corresponding to the ^{16}O isotopomer is presumably obscured by the 813/815 cm^{-1} peak. Thus, we are unable to ascertain the identity of this peak at the present time.

The Mössbauer analysis of **3b**(CPCA) favors its description as a species with predominantly Fe^{V}(O) character. However, the Raman bands observed for **2b**(PNA) and **3b**(PNA) fall into the low end of the relatively narrow range of frequencies (798–862 cm^{-1}) found for nonheme oxo–iron species described thus far.[50] The values at the extremes of this range are observed for [(bTAML)Fe^{IV}(O)]$^{2-}$ and [(bTAML)Fe^{V}(O)]$^{-}$, respectively, demonstrating a 64 cm^{-1} difference in frequency that presumably reflects the 1-unit change in oxidation state between the two complexes.[51] However, [(TMC)Fe^{IV}(O_{anti})-

DOI: 10.1021/jacs.7b11400
J. Am. Chem. Soc. XXXX, XXX, XXX–XXX

$(O_2CCF_3)]^+$ and $[(TMC)Fe^{IV}(O_{syn})(OTf)]^+$ exhibit respective Fe=O frequencies of 854 and 856 cm^{-1},[46,52] which approach that of $[(bTAML)Fe^{V}(O)]^-$, despite having a 1-unit lower oxidation state. This comparison suggests that the higher Fe=O frequencies of these three complexes may in fact arise from having a very weak ligand or no ligand at *all-trans* to the oxo group.[51,52] In contrast, $[(TMC)Fe^{V}(O)(NC(O)R)]^+$ and its conjugate acid have ν(Fe=O) values of 798 and 811 cm^{-1},[24] despite being considered to be Fe^{V}=O complexes. The lower frequencies of this acid/base pair have been suggested to reflect the strong electron donating character of the *trans*-imido ligand that weakens the Fe=O bond. These comparisons suggest caution in deducing the iron oxidation state based on the Fe=O frequency alone.

XAS studies were carried out on a sample containing **2**(CPCA) in frozen CH_3CN/acetone (v/v = 1:3). Table 3 compares the XAS results of **2**(CPCA) with those of its iron(II) precursor (**1**) and iron(III) decayed product. A K-edge energy of 7124.8 eV is observed (see Section XI of SI for details of this analysis), which is 1.6 eV higher than that found for $[(PyNMe_3)Fe^{II}(NCMe)_2]^{2+}$ (S = 0) in this study, but 0.5 eV lower than the 7125.3 eV value reported for both $[(TAML)Fe^{V}(O)]^-$ and $[(bTAML)Fe^{V}(O)]^-$ complexes.[18,51] The Mössbauer analysis of a sample from the same batch is described in section III of the SI (~50% **2b**(CPCA), 7% **2a**(CPCA), ~45% high-spin ferric species). To our surprise, the K-edge energy for the sample of **2**(CPCA) that had been allowed to decay at room temperature is within error essentially unchanged from that of **2**(CPCA) itself (7124.9 eV). However, the K-edge energy of 7124.9 eV found for decayed **2**(CPCA) falls within the range found for high-spin ferric centers, which can be as high as 7126.3 eV in coordination compounds.[53] Thus, given the overlap in the ranges for high-spin ferric centers and higher-valent complexes, the K-edge energy for **2**(CPCA) alone does not allow us to determine the iron oxidation state of the sample.

Analysis of the pre-edge region of **2**(CPCA) reveals a peak with an area of 15.6 units, a value smaller than typically found for nonheme oxoiron(IV) complexes (20−35 units).[50] It is also much smaller than the values of 52 and 65 units recently reported for the $[(bTAML)Fe^{IV}(O)]^{2-}$ and $[(bTAML)Fe^{V}(O)]^-$ complexes,[51] which reflect the square-pyramidal nature of the TAML-based complexes that leads to a significant distortion away from centrosymmetry. Thus, the iron centers in **2**(CPCA) are very likely six-coordinate.

Unlike the uninformative K-edge energy comparison between **2**(CPCA) and decayed **2**(CPCA), the corresponding EXAFS data comparison turn out to be more enlightening (Figure 6 and Table 3). The EXAFS analysis of **2**(CPCA) reveals the presence of an O scatterer at 1.63 ± 0.02 Å with an n value of 0.5, which is consistent with the Mössbauer-derived result that **2b**(CPCA) represents 50% of the sample. The short 1.63 Å distance falls within the narrow range of values ranging from 1.59 to 1.70 Å that are associated with high-valent terminal Fe=O complexes.[2,48,49] The values at the low and high ends of this range belong to the $Fe^{V}(O)$ and $Fe^{IV}(O)$ complexes of TAML and bTAML ligands, respectively.[18,51,54] DFT calculations presented in the following section provide an electronic structure picture that reconciles the apparent incompatibilities between the Raman and EXAFS results, which are at first glance suggestive of an Fe^{IV}=O unit, and the EPR and Mössbauer results that strongly favor an Fe^{V} oxidation state.

Table 3. XAS and EXAFS Analysis of 1, 2b(CPCA), and Decayed 2b(CPCA)

				EXAFS analysis		
	K-edge (eV)	pre-edge (eV)	pre-edge area (units)	N path	r (Å)	σ^2 ($\times 10^{-3}$)
1	7123.1	7112.8	4.9	3 N/O	1.9	4.8
				3 N/O	2.05	5.4
				6 C	2.85	2.8
				4 C	3.14	2.6
2b(CPCA)	7124.8	7114.4	15.6	0.5 N/O	1.63	1.4
				3 N/O	1.99	4.5
				2 N/O	2.17	6.2
				4 C	2.86	3.4
				4 C	3.00	3.5
decayed **2b**(CPCA)	7124.8	7114.3	14.3	3 N/O	2.02	5.3
				3 N/O	2.19	6.5
				6 C	2.97	8.5

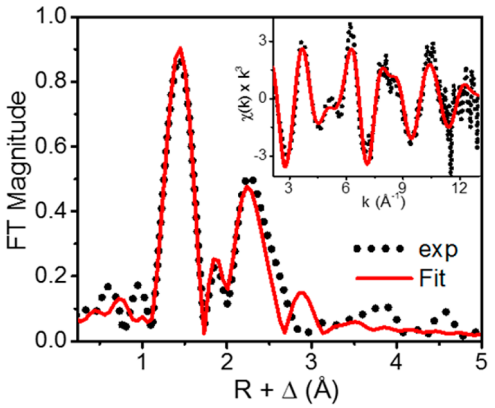

Figure 6. Unfiltered Fe K-edge EXAFS spectrum (black dotted line) and best fit (red solid line) of a sample containing 50% **2b**(CPCA). Inset: corresponding unfiltered k-space data (black dots) and best fit (red line). See Table 3 and section XI in the SI for further details.

DFT Studies and Discussion. To provide insight into the electronic structure of **3b**(CPCA), we have carried out a series of DFT calculations. For the reported studies of $[(TMC)Fe^{V}(O)(NC(OH)CH_3)]^{2+}$ we used the BP86 functional because the hybrid B3LYP functional favored an Fe^{IV}=O/radical state that gave an ^{57}Fe A-tensor inconsistent with the experimental data.[24] In contrast, the BP86 functional produced, for reasons understood, a solution with substantial Fe^{V}=O character that rationalized the set of experimental observations. Consequently, we have used here the BP86 functional for all calculations on **3b**(CPCA).

We have carried out geometry optimizations for **3b**(CPCA) (Figure 7) and a variety of related complexes (see details in Table 4). To compare the unperturbed Fe−oxo bond length in different oxidation states, we have also optimized the structures of the two $[(MeO\text{-}PyNMe_3)Fe(O)(NCMe)]^{n+}$ complexes (n = 2, 3) and obtained a 1.67 Å Fe=O distance for the Fe^{IV} state and a 1.63 Å Fe=O distance for the Fe^{V} state (Table 4). Mössbauer spectra for $[(PyNMe_3)Fe^{IV}(O)(NCMe)]^{2+}$, **4**, are presented in section IV of the SI. Geometry optimization attempted for the peroxo species **2a**(PAA) and **3a**(CPCA) with BP86 resulted in minimized structures for the corresponding

DOI: 10.1021/jacs.7b11400
J. Am. Chem. Soc. XXXX, XXX, XXX−XXX

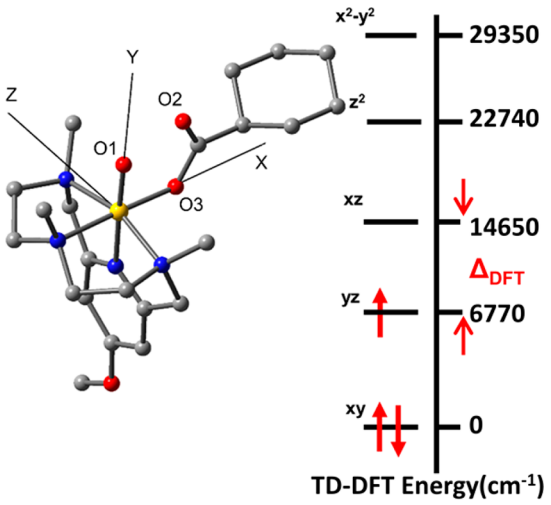

Figure 7. Geometry-optimized structure of $[(MeO\text{-}PyNMe_3)Fe^{V}(O)(OC(O)cy)]^{2+}$ (**3b**(CPCA), *trans* isomer): Yellow, iron; red, oxygen; blue, nitrogen; gray, carbon. For clarity, hydrogen atoms are not shown. Electronic d-orbital diagram obtained from TD-DFT is shown and the Δ_{DFT} is about 8000 cm^{-1}. Selected bond lengths: Fe=O 1.65 Å; O1–O2 = 2.04 Å; Fe–O3 = 1.93 Å; Fe–N_{pyr} = 1.97 Å, Fe–N_{am} ≈ 2.08 Å. The DFT coordinates x, y, z match the coordinates used for the spin Hamiltonian analysis, eqs 1, to within a few degrees. TD-DFT computations were performed for the optimized structure including 50 excited states. The energy of the d_{yz} orbital was obtained from the excitation of the β electron from d_{xy} to d_{yz}. The energies of other orbitals (d_{xz}, d_{z2}, d_{x2-y2}) were obtained from the excitation of the α electron from the δ_{yz} orbital to these orbitals.

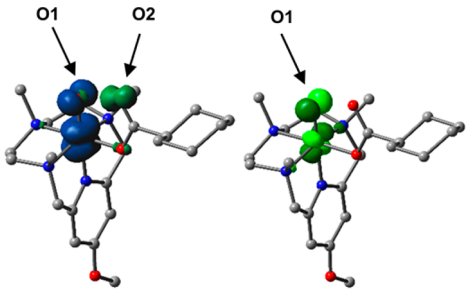

Figure 8. Spin density plot (left) and α HOMO (right) of BP86 solution of the *trans* isomer of $[(MeO\text{-}PyNMe_3)Fe^{V}(O)(OC(O)cy)]^{2+}$ (**3b**(CPCA)). Majority spin α in blue; minority spin β (mainly on O2) in dark green in the left cartoon.

526 Fe^{V}=O isomers, whereas the B3LYP optimization yielded a
527 solution for the peroxo isomer **3a**(CPCA), $[(MeO\text{-}PyNMe_3)$-
528 $Fe^{III}(\kappa^2\text{–}OOC(O)cy)]^{2+}$.

529 For the $PyNMe_3$ and $MeO\text{-}PyNMe_3$ ligands, geometry
530 optimizations of the corresponding high-valent iron–oxo
531 complexes yielded two isomers with rather similar properties
532 that reproduce the experimental data very well (see section VII
533 of the SI for a comparison of the calculated properties). One
534 isomer has the oxo group *trans* to the pyridine, whereas the
535 other assumes the *cis* configuration. The α HOMO of both
f8 536 optimized structures (Figures 8 and Figure S29) has
537 approximate d_{yz} symmetry and the normal of the orbital
538 plane in both isomers is directed toward the bound carboxylate
539 oxygen, with *z* essentially parallel to the Fe-oxo direction. The
540 main text focuses on the *trans* isomer of **3b**(CPCA), which is
541 calculated to be 0.6 kcal/mol lower in energy than its *cis*
542 analogue. A corresponding α HOMO and a spin density plot of
543 the *cis* isomer are shown in Figure S29.

544 The calculated Fe=O bond length of 1.65 Å for **3b**(CPCA)
545 agrees within the error with the 1.63 ± 0.02 Å value obtained
546 by EXAFS. This value is larger than the 1.59 Å distance
547 observed for the 5-coordinate $[(TAML)Fe^{V}(O)]^{-}$;[18] distances
548 calculated by DFT using B3LYP and BP86 yielded 1.59 and
549 1.60 Å, respectively. In section IX of the SI, we considered the
550 hypothetical 6-coordinate $[(TAML)Fe^{V}(O)(NCMe)]^{-}$, for
551 which a relaxed scan was performed along the Fe–N_{MeCN}
552 distance. These calculations suggest that if the TAML complex
553 were 6-coordinate, it would have had an Fe^{V}=O bond length
554 of ∼1.63 Å. We have also optimized the structures of the two
555 $[(MeO\text{-}PyNMe_3)Fe(O)(NCMe)]^{n+}$ complexes (n = 2, 3),
556 obtaining 1.67 Å for the Fe^{IV} state and 1.63 Å for the Fe^{V} state
557 (Table 4). Thus, the 1.63 Å observed here by EXAFS is
558 consistent with BP86 structures for 6-coordinate (MeO-
559 $PyNMe_3)Fe^{V}$ species. The calculated properties are hardly
560 affected by the MeO substitution; see Table S5.

561 Interestingly, in **3b**(CPCA) the non-iron-bound carboxylate
562 oxygen (O2) is close to the oxo group, O1, with an O1–O2
563 distance of 2.04 Å. It is noteworthy that the spin density plot of
564 Figure 8 shows *negative* spin density at O2, indicating that the

Table 4. DFT Values for Spin Populations, $n = n_\alpha - n_\beta$, of Orbitals and atoms, ^{57}Fe Isomer Shifts, Bond Lengths, and Raman Frequencies of the Iron–Oxo Bond for 3b(CPCA) and Related Complexes

	$[(L^*)Fe^{V}(O)\text{-}(OC(O)cy)]^{2+}$ (3b(CPCA))[a] *trans* (*cis*)	$[Fe^{V}(O)\text{-}(TAML)]^{-}$[b]	$[(L^*)Fe^{IV}(O)\text{-}(NCMe)]^{2+}$ *trans*	$[(L^*)Fe^{V}(O)\text{-}(NCMe)]^{3+}$ *trans* (*cis*)	$[(L^*)Fe^{III}\text{-}(\kappa^2\text{–}OOC(O)cy)]^{2+}$ *cis*[d]
Fe–O1 bond (Å)	1.65 (1.66)	1.60	1.67	1.63 (1.63)	1.82
isomer shift[e] (mm/s)	−0.01(−0.02)	−0.40	+0.05	−0.12 (−0.14)	+0.26
ν(Fe–O1) (cm^{-1})	837 (815)	875	841	903 (875)	
ν(O1–O2) (cm^{-1})					789 and 732[f]
$\langle S^2 \rangle$	0.84	0.76	2.01	0.94[c]	0.77
{Fe-d_{xz} + O1-p_x}	0.12	0.07	0.87	0.26	0.04
{Fe-d_{yz} + O1-p_y}	0.90	0.84	0.89	0.89	0.57
O2	−0.18	N/A	N/A	N/A	0.00

[a]L* = $(MeO\text{-}PyNMe_3)$ [b]Parameters obtained with BP86/6-311G [c]The *trans* isomer (oxo group *trans* to the pyridine) did not optimize in the Fe^{III} state using either the B3LYP or BP86 functional. The *cis* isomer of this column was optimized using B3LYP/6-311G but did not optimize with BP86. Calculated O1–O2 bond length is 1.54 Å. [d]The DFT solution may be admixed with a small amount ofS = 3/2 Fe^{V}. [e]The calculated isomer shifts were obtained by the method of Vrajmasu et al.[55] [f]The two modes also have significant cyclohexyl character.

DOI: 10.1021/jacs.7b11400
J. Am. Chem. Soc. XXXX, XXX, XXX–XXX

Fe^{V} ground state of **3b**(CPCA) is admixed with an Fe^{IV}/radical configuration. An indirect measure for the oxidation state of iron in the DFT solution is the expectation value of the operator $\mathbf{S}^2$. For a pure Fe^{V} $S = 1/2$ state this expectation value would be $\langle S = 1/2|\mathbf{S}^2|S = 1/2\rangle = S(S + 1) = 0.75$, whereas the Fe^{IV}/carboxyl radical broken-symmetry (BS) configuration would yield $\langle BS|\mathbf{S}^2|BS\rangle = 1.75$. If we assume that only these two configurations contribute, we would infer from the calculated $\langle \Psi_{BP86}|\mathbf{S}^2|\ \Psi_{BP86}\rangle = 0.85$ that the ground state of **3b**(CPCA) is 90% Fe^{V}. This argument may be somewhat misleading as the $S = 1/2$ $[(MeO\text{-}PyNMe_3)Fe^{III}(\kappa^2\text{-}OOC(O)cy)]^{2+}$ configuration may also contribute; we comment on this point below.

The Fe^{V} assignment of **3b**(CPCA) is supported by the spin densities of the key orbitals in Table 4. Note that the $d_{yz}+p_y$ and $d_{xz}+p_x$ populations are nearly equal for the $S = 1$ $[(MeO\text{-}PyNMe_3)Fe^{IV}(O)(NCMe)]^{2+}$ complex but that the $d_{xz}+p_x$ population is substantially smaller than the $d_{yz}+p_y$ population for the two Fe^{V} complexes. (This statement requires a caveat. Thus, the relatively long Fe−O1 bond in $[(MeO\text{-}PyNMe_3)Fe^{III}(\kappa^2\text{-}OOC(O)R)]^{2+}$ leads to an interchange of the d_{xz} and d_{yz} orbitals, which puts the unpaired electron of the low-spin Fe^{III} into d_{yz}. Admixture of the latter state into the Fe^{V} state would have little effect on the **A** tensor.)

The predominant Fe^{V} nature of **3b**(CPCA) is also evident from the isomer shifts, δ. The experimental value for $[(MeO\text{-}PyNMe_3)Fe^{V}(O)(OC(O)cy)]^{2+}$ is $\delta = -0.08$ mm/s; the BP86 values are −0.01and −0.02 mm/s for the *trans* and *cis* isomers, respectively. For $[(PyNMe_3)Fe^{IV}(O)(NCMe)]^{2+}$ (**4**) (see section IV of the SI), we experimentally obtained $\delta = +0.05(1)$ mm/s with Mössbauer spectroscopy, which is accurately reproduced (Table 4) by the BP86 calculation. For the hypothetical $[(MeO\text{-}PyNMe_3)Fe^{V}(O)(NCMe)]^{3+}$ complex, a BP86 calculation yielded $\delta = -0.14$ mm/s. The B3LYP functional optimizes the *cis* isomer of $[(MeO\text{-}PyNMe_3)Fe^{III}(\kappa^2\text{-}OOC(O)R)]^{2+}$ to a peroxo-bound Fe^{III} state with $\delta = +0.26$ mm/s, which is close to the experimental +0.23 mm/s of the $[(TPA^*)Fe^{III}(OOC(O)CH_3)]^{2+}$ complex of Oloo et al.[37] To explain its low isomer shift, the iron center in **3b**(CPCA) must be substantially more oxidized than those in $[(MeO\text{-}PyNMe_3)Fe^{III}(\kappa^2\text{-}OOC(O)R)]^{2+}$ and **4**, again giving support to the Fe^{V} assignment for **3b**(CPCA). The experimental $\delta = -0.08$ mm/s is more negative than the BP86 value of −0.01 mm/s, suggesting that the calculation has perhaps overestimated the (Fe^{IV}/radical)/(Fe^{III}-peroxo) content of the state. (Note that complex **4**, for which we have a δ, has the $PyNMe_3$ ligand. Our DFT studies suggest that the methoxy substitution would not affect the value of δ, see Table S5.)

Above we indicated that the ground state of **3b**(CPCA) may contain a small Fe^{III}−peroxo admixture. A qualitative argument sheds some light on this possibility. As shown in Table 4, the calculated isomer shift of $[(MeO\text{-}PyNMe_3)Fe^{V}(O)(NCMe)]^{3+}$ (see Figure S27) is $\delta = -0.14$ mm/s. The calculated $\langle \mathbf{S}^2\rangle = 0.96$ for this complex suggests that the $S = 1/2$ ground state may have a small (∼4%) high-spin ($S = 3/2$) Fe^{V} admixture. However, this contamination is too small to affect the calculated δ significantly. In the following analysis we adopted for the $[(MeO\text{-}PyNMe_3)Fe^{IV}(^{\bullet}OCOcy)]^{2+}$ and $(MeO\text{-}PyNMe_3)Fe^{III}$-peroxo configurations the experimentally observed value $\delta = +0.05$ mm/s for $[(PyNMe_3)Fe^{IV}(O)(NCMe)]^{2+}$ (**4**) and the DFT value $\delta = +0.26$ mm/s (Table 4), respectively. If the ground state of **3b**(CPCA) would comprise 90% Fe^{V} and 10% Fe^{IV}/radical, but no Fe^{III}−peroxo admixture, we would obtain a δ value near −0.12 mm/s, which is lower than the experimentally observed −0.08 mm/s. Using the isomer shifts listed in Table 4 and assuming that the ground state wave function of **3b**(CPCA) is an admixture of Fe^{V}=O (75%), Fe^{IV}=O/radical (15%) and Fe^{III}−peroxo (10%) a δ-value close to the experimental $\delta = -0.08$ mm/s is obtained ($\delta = (0.10 \times 0.26 + 0.15 \times 0.05 + 0.75 \times (-0.14))$ mm/s = −0.07 mm/s). A similar qualitative estimate rationalizes the experimentally determined $\nu_{Fe=O}$. From the perspective of bond order, we calculated the Wiberg bond orders of Fe=O1 and O1−O2 in **3b**(CPCA). These calculations show that **3b**(CPCA) has an O1−O2 bond order of 0.35, indicating that the peroxo bond is not entirely ruptured, which supports the mixing of Fe^{III}-peroxo and Fe^{V}=O components in **3b**(CPCA). For comparison, we have also calculated the Fe−O bond orders of **3a**(CPCA), $[Fe^{IV}(O)(TAML)]^{2-}$, $[Fe^{V}(O)(TAML)]^{-}$, and the hypothetical $[(MeO\text{-}PyNMe_3)Fe^{IV}(O)(NCMe)]^{2+}$ complex (see Table S10).

The DFT calculated **g** and **A** tensors have a common z-axis which is within 4° of the Fe−oxo direction, and the x-axis of the **A** tensor is along the Fe−O3 bond. The principal axes of the **g** tensor are rotated by $\alpha = 26°$ around z relative to the frame for **A**. The close agreement with the experimental ($\alpha = 20°$) value for this angle is probably a bit fortuitous. The DFT-calculated g-values of **3b**(CPCA) reproduce the experimental data quite well; it is noteworthy that the largest component of the **A** tensor is closely aligned with the axis for $g_{mid} = g_y$, just as found experimentally.

The ^{57}Fe magnetic hyperfine tensor, **A**, has Fermi contact (A^{FC}), anisotropic spin-dipolar (A^{SD}), and orbital (A^{L}) contributions. From the experimental $A_{x,y,z} = (-62, -8, -9)$ MHz we obtain $A_{iso} = (A_x + A_y + A_z)/3 = -26.3$ MHz. In order to extract A^{FC} we should subtract the isotropic part of A^{L} from A_{iso}. The closeness of the g-values of **3b**(CPCA) to $g = 2.00$ implies that this contribution is small. The DFT calculation for the *trans* isomer yields $A^{L}_{x,y,z} = (-3.4, +2.5, -0.3)$ MHz from which follows that $A^{L}_{iso} = -0.4$ MHz and therefore $A_{iso} - \mathbf{A}^{L}_{iso} = A^{FC} = -25.9$ MHz. DFT calculations often underestimate the magnitude of the Fermi contact term, requiring the DFT-calculated A^{FC} values to be multiplied by 1.6 to match the experimental A^{FC}.[56] However, the $A^{FC}(DFT) = -18.6$ MHz obtained for the *trans* conformer suggests a smaller correction factor, $A^{FC}/A^{FC}(DFT) = 1.42$. The value $A^{FC} = -25.9$ MHz deduced for **3b**(CPCA) is substantially larger than the $A_{FC} = -21.7$ MHz obtained for $[(TAML)Fe^{V}(O)]^{-}$. This increase may possibly be due to the admixture of the Fe^{IV}/radical configuration into the Fe^{V} ground state, thereby increasing the internal magnetic field at the ^{57}Fe nucleus. As the simulations of the Mössbauer spectra are based on an $S = 1/2$ Hamiltonian, the increase in the internal field would have to be accounted for by a larger value for A^{FC}.

While the methoxy substituent on the supporting ligand affects the equilibrium concentrations between the Fe^{V}=O and Fe^{III}-peroxo forms (ratio 7:1 for $PyNMe_3$ and 50:1 for $MeO\text{-}PyNMe_3$), the calculated properties evaluated above are essentially insensitive to the substitution (see Table S5). Moreover, the EPR parameters for **2b**(PAA), **2b**(CPCA), and **3b**(CPCA) are the same and, within the experimental errors, the Mössbauer parameters of **2b**(CPCA) and **3b**(CPCA) are also the same. Note, however, that λ_{max} of the UV−vis absorption feature of **3b**(CPCA) (λ_{max} 520 nm) is red-shifted

DOI: 10.1021/jacs.7b11400
J. Am. Chem. Soc. XXXX, XXX, XXX−XXX

relative to that of **2b**(CPCA) (λ_{max} 505 nm),[43] presumably due to the presence of the MeO substituent in **3b**(CPCA).

The Raman spectrum of **2**(PNA) exhibits two features at 815 and 829 cm^{-1} (11:1 intensity ratio), which disappear when **2**(PNA) decays (see Figure S32 in the SI). Both features fall within the range of frequencies typically observed for Fe^{IV}=O complexes.[50] We note that similarly low Fe=O frequencies of 798 and 811 cm^{-1} have been observed for $[(TMC)Fe^{V}(O)(NC(O)CH_3)]^{+}$ and $[(TMC)Fe^{V}(O)(NC(OH)CH_3)]^{2+}$, Fe^{V}=O complexes with an electronic structure quite similar to that of **2b**(PAA), **2b**(CPCA), and **3b**(CPCA). The low ν(Fe=O) values for the two TMC complexes were rationalized by the *trans* effect of the imido ligand.[24] For **2b**(CPCA) and **3b**(CPCA), the oxo group is perturbed by residual bonding to O2. The effect of this perturbation can be seen by comparing the ν(Fe=O) values listed in Table 4. Thus, $[(MeO\text{-}PyNMe_3)Fe^{V}(O)(NCMe)]^{3+}$ and $[(TAML)Fe^{V}(O)]^{-}$ are calculated to have ν(Fe=O) = 903 and 875 cm^{-1}, respectively, compared to an experimental value of 862 cm^{-1} reported for $[(bTAML)Fe^{V}(O)]^{-}$.[51] On the other hand, calculations for **2b**(CPCA) and **3b**(CPCA) yield values of 836 and 815 cm^{-1} for the *trans* and *cis* isomers, respectively, with the latter value being observed experimentally for **2b**(CPCA) (Figure 5). The downshifts of these values from ~903 cm^{-1} are probably caused by the perturbation of the Fe=O1 oscillator by interactions with O2. Thus, while the ν(Fe=O) of *unperturbed* Fe=O oscillators are good indicators of the oxidation state of the iron,[50] the lower Raman frequencies of **2b**(CPCA) and **3b**(CPCA) reflect the presence of interactions between the oxo group and O2 of the partially cleaved peroxo bond.

■ CONCLUSIONS AND PERSPECTIVES

Complex **1** is a truly remarkable nonheme iron catalyst that uses peracetic acid as oxidant to generate a high-valent intermediate that hydroxylates cyclohexane at −40 °C at a record breaking rate of 2.8 M^{-1} s^{-1}.[1] This rate is 10^4-fold faster than that found for the well characterized bona fide oxoiron(V) complex $[Fe^{V}(O)(TAML)]^{-}$.[18,23,51] This large difference in reactivity can be rationalized by the use of the neutral $PyNMe_3$ as a supporting ligand compared to the tetraanionic TAML ligand in the latter that significantly mitigates the high electrophilicity of the Fe^{V}=O unit (see Table S11).

This metastable high-valent intermediate accumulates at lower temperature, permitting its characterization by a variety of spectroscopic methods. By replacing the $PyNMe_3$ ligand of **1** with MeO-$PyNMe_3$ and changing the peracetic acid oxidant to cyclohexyl peroxycarboxylic acid, we have been able to obtain the S = 1/2 intermediate $[(MeO\text{-}PyNMe_3)Fe^{V}(O)(OC(O)cy)]^{2+}$, **3b**(CPCA), in sufficient purity to allow its detailed characterization by Mössbauer spectroscopy. Intermediate **3b**(CPCA) has an isomer shift δ = −0.08 mm/s, which is 0.13 mm/s more negative than that measured for $[(PyNMe_3)Fe^{IV}(O)(NCMe)]^{2+}$ (**4**). Our spectroscopic studies thus show that **3b**(CPCA) has an electronic structure with predominant Fe^{V} character.

DFT calculations on **3b**(CPCA) reveal a species with a rather unusual geometric and electronic structure that affords spectroscopic parameters reasonably matching those obtained experimentally. A notable feature of this structure, which applies for **2b**(PAA), **2b**(CPCA) and **3b**(CPCA), is the O1···O2 distance of ~2.04 Å obtained from DFT calculations. This unique structure keeps the carboxylate O2 in close proximity to the Fe=O unit, enabling the complex to maintain in solution a facile equilibrium between the Fe^{V}=O and Fe^{III}-peroxo forms, as described by Serrano-Plana et al. for **2a**/**2b**;[43] for **3**(CPCA) this equilibrium is shifted heavily in favor of **3b**(CPCA). Given that the ground state of **3b**(CPCA) has some Fe^{IV}(O)− carboxyl radical and perhaps also some Fe^{III}−peroxo character admixed into the dominant Fe^{V}(O) nature of the intermediate, it might appear that **3b**(CPCA) is a species with a nearly severed peroxo bond that is more stable than both its limiting acylperoxoiron(III) or its oxoiron(V) isomers. However, a relaxed scan of the O1−O2 distance shows that the increase of r(O1−O2) does not further enhance the calculated Fe^{V} character of **3b**(CPCA) but in fact results in an increase of Fe^{IV}-radical character as the O1−O2 bond becomes cleaved homolytically. This result suggests that the above-described electronic structure of **3b**(CPCA) has as much Fe^{V} character as the system will allow at the BP86 level of theory. Clearly, additional theoretical studies are desirable, but the present work indicates how its oxidative power might arise in an unexpectedly subtle manner along the O−O bond stretching reaction coordinate. This notion may hold the key to understanding the high reactivity of **3b**(CPCA) as a C−H bond cleaving species.

The $PyNMe_3$-derived intermediates **2** and **3** described in this paper are the latest variants in a series of proposed Fe^{V}(O) oxidants that have been postulated to be the actual C−H bond leaving agents in the chemistry of a number of nonheme iron catalysts, including some that are found to be useful for late-stage oxidations of natural products and pharmaceuticals.[57−60] For the Fe(TPA) catalyst (TPA = tris(pyridyl-2-methyl)amine) used in combination with H_2O_2 as oxidant, an $[(TPA)Fe^{III}$−OOH] intermediate is observed to form at −40 °C and then undergoes rate-determining O−O bond cleavage to unmask the proposed $[(TPA)Fe^{V}(O)(OH)]$ oxidant responsible for alkane hydroxylation and olefin epoxidation and *cis*-dihydroxylation.[61] On the other hand, for the related Fe(TPA*) catalyst (TPA* = tris(4-methoxy-3,5-dimethylpyridyl-2-methyl)amine) in combination with the H_2O_2 oxidant and excess HOAc additive, a $[(TPA^*)Fe^{III}(O_3CR))]$ intermediate is generated instead.[37,62] Kinetic analysis of the behavior of this intermediate at −40 °C in the presence of various substrates suggests that this species is in equilibrium with a small concentration of the actual oxidant, proposed to be a $[(TPA^*)Fe^{V}(O)(OAc)]$ species.[37,62] The latter has in fact been identified by Talsi as giving rise to a minor g = 2.07 EPR signal that decays at a rate dependent on substrate concentration.[35,63] This signal is essentially identical to that associated with the major EPR-active components of **2** and **3** reported in this paper. Thus, in the series of polydentate ligands from TPA to MeO-$PyNMe_3$ that support bioinspired nonheme iron catalysts discussed in this paper, the notion of an Fe^{V}=O oxidant has progressed from mere hypothesis in Fe(TPA) catalysis to being detected as a minor component in the Fe(TPA*)/H_2O_2/HOAc system and then now to becoming the predominant species observed at −40 °C in the Fe(MeO-$PyNMe_3$)/peracid combination with detailed spectroscopic characterization.

The S = 1/2 intermediates associated with the above systems, namely $[(TPA)Fe^{III}(OOH)]$, $[(TPA^*)Fe^{III}(O_3CR)]$, **2b** and **3b**, all exhibit visible absorption features around 500 nm, but they progressively increase in intensity in the series with molar extinction coefficients of ~1000 for $[(TPA)Fe^{III}(OOH)]$,[64] ~2500 for $[(TPA^*)Fe^{III}(O_3CR)]$,[37] ~4500 for **2b**, and ~7500 for **3b**. We do not yet understand the basis for this trend of

DOI: 10.1021/jacs.7b11400
J. Am. Chem. Soc. XXXX, XXX, XXX−XXX

increasing intensity, but suggest that the higher absorptivity reflects the increasing fraction of the $g = 2.07$ species present in the reaction mixtures, which we attribute the unusual electronic structures of **2b** and **3b**. The observation that there is a significant change in extinction coefficient between **2b** and **3b** as a result of a 4-OMe substitution on the pyridine of the supporting ligand suggests that the pyridine must be involved in this chromophore Further investigation is required to gain insight into this phenomenon.

What makes the highly reactive intermediates **2b** and **3b** reported in this paper truly extraordinary is the fact that they represent 40−50% of the Fe in the catalytic mixture and are found to be catalytically competent in the C−H bond cleavage, as evidenced by the dependence of their decay on the nature and concentration of substrate.[43] The DFT-based electronic structure that we describe here for **2b** and **3b** may at first glance appear to most readers to be a transition state in the homolytic cleavage of the O−O bond of an acylperoxoiron(III) complex, but our calculations find an energy minimum at an O···O distance of 2.04 Å with a calculated Wiberg O−O bond order of 0.35. Only such a structure thus far reproduces the spectroscopic data collected for **2** and **3**. Decreasing the O−O bond beyond 2.04 Å leads to the acylperoxoiron(III) electromer, while stretching the O−O bond beyond 2.04 Å evolves the system toward the $(N_4)Fe^{IV}(O)(^{\bullet}OC(O)R)$ electromer (see Figure S46) upon complete O−O bond homolysis. According to our DFT calculations, it is at the 2.04-Å O···O distance where the $Fe^{V}(O)$ character of the intermediate is maximized. Thus, we speculate that this oxidation-state buffering mechanism stabilizes this species and allows it to accumulate and be observed.

EXPERIMENTAL SECTION

Materials. Reagents and solvents used were of commercially available reagent quality unless otherwise stated. Solvents were purchased from Scharlab, Acros or Sigma-Aldrich and used without further purification. Peracetic acid (PAA) was purchased from Aldrich as a 32 wt % solution in acetic acid containing less than 6% H_2O_2. Cyclohexanyl peroxycarboxylic acid (CPCA) was prepared following previously described procedures.[65] 95% ^{18}O-labeled H_2O_2 (28% w/w in H_2O) was purchased from Gioxcat. Preparation and handling of air-sensitive materials were carried out in a N_2 drybox (Jacomex) with O_2 and H_2O concentrations <1 ppm. The synthesis of MeO-PyNMe$_3$ and its iron complex are detailed in the Supporting Information. (See the regular sample preparations in section I of the SI, and see the ^{18}O-labeled sample preparations in Section XII of the SI.)

Generation of 2b(PAA), 2b(CPCA), 2b(PNA) and 3b(CPCA). In a typical experiment, a 4 mM solution of $[(PyNMe_3)Fe^{II}(CF_3SO_3)_2]$ (**1**) or $[(MeO\text{-}PyNMe_3)Fe^{II}(CF_3SO_3)_2]$ (**1′**) in dry acetonitrile was prepared inside the glovebox.A 0.5 mL portion of this solution was placed in a UV−vis cuvette (2 μmols), and 1.5 mL of dry acetone was added. The quartz cell was capped with a septum and taken out of the box, placed in the Unisoku cryostat of the UV−vis spectrophotometer, and cooled to 223 K. After reaching thermal equilibrium, a UV−vis spectrum of the starting complex was recorded. Then, 50 μL of a solution containing the desired amount of alkyl peracid in dry acetonitrile were added, giving raise to the formation of the characteristic UV−vis bands of **2b**(PAA), **2b**(PNA), **2b**(CPCA), or **3b**(CPCA).

Mössbauer and EPR samples of **3b**(CPCA) were generated as follows. A 1 mM solution of $[(MeO\text{-}PyNMe_3)Fe^{II}(CF_3SO_3)_2]$ in 3:1 acetone/MeCN was transferred into a 1 cm path length optical cuvette and cooled in a Unisoku cryostat to −70 °C, and then a 10-fold excess of CPCA was added. The reaction was stopped by freezing near maximal development of the 520 nm band. At−70 °C the half-life of the decay of **3b**(CPCA) is longer than 1 h.

Generation of 4. A 4 mM solution of $[(PyNMe_3)Fe^{II}(CF_3SO_3)_2]$ in dry acetonitrile was prepared inside the glovebox. A 0.5 mL of this solution was placed in a UV−vis cuvette (2 μmol), and 1.5 mL of dry acetone was added. The quartz cell was capped with a septum and taken out of the box, placed in the Unisoku cryostat of the UV−vis spectrophotometer, and cooled to 233 K. After reaching thermal equilibrium, 50 μL of a solution containing 2-^{t}BuSO$_2$−C$_6$H$_4$IO (8 μmols) was added.

Physical Methods. Mössbauer spectra were recorded with two spectrometers using Janis Research (Wilmington, MA) SuperVaritemp dewars that allow studies in applied magnetic fields up to 7.5 T in the temperature range from 1.5 to 200 K. Mössbauer spectral simulations were performed using the WMOSS software package (SEE Co, Edina, MN). Perpendicular (9.63 GHz) mode X-band EPR spectra were recorded on a Bruker EPP 300 spectrometer equipped with an Oxford ESR 910 liquid helium cryostat and an Oxford temperature controller. The quantification of the signals was relative to a Cu-EDTA spin standard. Software for EPR analysis, SpinCount, was provided by Prof. M. P. Hendrich of Carnegie Mellon University. The spin quantitation error is about 8−10%.

Resonance Raman spectra were obtained with excitation at 515 nm (50 mW at source, Cobolt Lasers) and 561 nm (100 mW at source, Cobolt Lasers). Data were obtained on samples at 77 K on frozen samples in NMR or EPR tubes using a 135° backscattering arrangement. The collimated Raman scattering was collected using two Plano convex lenses ($f = 12$ cm, placed at an appropriate distance) through appropriate long pass edge filters (Semrock) into an Acton AM-506M3 monochromator equipped with a Princeton Instruments ACTON PyLON LN/CCD-1340 × 400 detector. The detector was cooled to −120 °C prior to the experiments. Spectral calibration was performed using the Raman spectrum of acetonitrile/toluene 50:50 (v:v).[66] Each spectrum was typically accumulated over 30−40 scans with 1 s acquisition time, resulting in a total acquisition time of 30−40 s per spectrum. The collected data was processed using Spekwin32,[67] and a multipoint baseline correction was performed for all spectra. The two 800 cm^{-1} features were fitted using the Fityk software with pseudo-Voigt functions composed of 50:50 Gaussian/Lorentzian functions.

Fe K-edge X-ray absorption spectra on the frozen solution of **2b**(CPCA), decayed **2b**(CPCA), and species **1** were collected at 10 K in the energy range 6900 to 8000 eV on the Beamlines 9-3 at the Stanford Synchrotron Radiation Lightsource (SSRL) of SLAC National Accelerator Laboratory. One hundred element solid-state Ge detectors (Canberra) were used to obtain the X-ray absorption spectroscopy (XAS) data on the Beamline 9-3. An iron foil was used for the energy calibration of the beam and the first inflection point of the edge assigned to 7112.0 eV. Six scans of the fluorescence excitation spectra were collected on all the samples. To increase the signal-to-noise ratio of the spectra, a 3 μm Mn filter along with a solar slit were placed in between the detector and the sample. Data reduction, averaging, and normalization were performed using the program EXAFSPAK. The pre-edge features were fitted using the Fityk software with pseudo-Voigt functions composed of 50:50 Gaussian/Lorentzian functions.

DFT calculations were performed using the BP86 functional and 6-311G basis set by Gaussian '09 (revision D.01) and ORCA (3.0.3). The former is used for geometry optimization, time-dependent density-functional calculations, and Raman frequency calculations; the latter was used for spin Hamiltonian parameter calculation. Self-consistent field and geometry calculations were performed with default convergence criteria.

ASSOCIATED CONTENT

Supporting Information

The Supporting Information is available free of charge on the ACS Publications website at DOI: 10.1021/jacs.7b11400.

Sample preparation details and NMR characterization; spectral simulations for contaminating high-spin ferric species; Mössbauer and EPR data and analysis for

DOI: 10.1021/jacs.7b11400
J. Am. Chem. Soc. XXXX, XXX, XXX−XXX

2b(CPCA) and **2b**(PNA); Mössbauer spectra for **4**; additional DFT structures and coordinates; Raman spectra and XAS analyses; synthesis of ^{18}O enriched PNA; bond order analysis; Raman spectra comparison with varying type of ligands and peroxy acids(PDF)
X-ray data for complex **1** (CIF)

AUTHOR INFORMATION

Corresponding Authors

*emunck@cmu.edu
*larryque@umn.edu
*miquel.costas@udg.edu
*eb7g@andrew.cmu.edu
*ysguo@andrew.cmu.edu
*enrique.garcia-es@uv.es

ORCID

Vlad Martin-Diaconescu: 0000-0002-7575-2237
Yisong Guo: 0000-0002-4132-3565
Emile L. Bominaar: 0000-0002-5125-265X
Lawrence Que Jr.: 0000-0002-0989-2813
Miquel Costas: 0000-0001-6326-8299
Eckard Münck: 0000-0002-1867-0358

Present Addresses

#(J.S.-P.): University of Basel, Department of Chemistry, Mattenstrasse 24a building BPR 1096, CH-4058 Basel, Switzerland.
⊗(W.N.O.): 9617 Bald Hill Road, Bowie, MD 20721.

Notes

The authors declare no competing financial interest.

ACKNOWLEDGMENTS

The work at Carnegie Mellon University was supported by the US National Science Foundation (CHE-1305111 to E.M. and CHE-1654060 to Y.G.). The work at the University of Minnesota was supported by National Science Foundation grants (CHE-1361773 and CHE-1665391, L.Q.). The work at the University de Girona was supported by the Spanish Ministry of Science CTQ2015-70795-P (M.C.) and CTQ2016-77989-P) (A.C.). The studies at the University of Valencia received financial support from the Spanish Ministerio de Economía y Competitividad (Project CTQ2016-78499-C6-1-R and Unidad de Excelencia MDM 2015-0038) and Generalitat Valenciana (Project PROMETEOII2015-002). XAS data were collected on a Beamline 9-3 at the Stanford Synchrotron Radiation Lightsource, SLAC National Accelerator Laboratory. SLAC is supported by the U.S. Department of Energy (DOE), Office of Science, Office of Basic Energy Sciences under Contract No. DE-AC02-76SF00515. Use of the Beamline 9-3 is supported by the DOE Office of Biological and Environmental Research and the National Institutes of Health, National Institute of General Medical Sciences (including P41GM103393). We thank Professor Michael P. Hendrich for valuable help with our EPR work. We appreciate illuminating discussions with Dr. Shengfa Ye on computational aspects of the present work.

REFERENCES

(1) Hohenberger, J.; Ray, K.; Meyer, K. *Nat. Commun.* **2012**, *3*, 720.
(2) McDonald, A. R.; Que, L. *Coord. Chem. Rev.* **2013**, *257*, 414−428.
(3) Ray, K.; Pfaff, F. F.; Wang, B.; Nam, W. *J. Am. Chem. Soc.* **2014**, *136*, 13942−13958.
(4) Groves, J. T. *J. Inorg. Biochem.* **2006**, *100*, 434−447.
(5) Huang, X.; Groves, J. T. *JBIC, J. Biol. Inorg. Chem.* **2017**, *22*, 185−207.
(6) Sahu, S.; Goldberg, D. P. *J. Am. Chem. Soc.* **2016**, *138*, 11410−11428.
(7) Kovaleva, E. G.; Lipscomb, J. D. *Nat. Chem. Biol.* **2008**, *4*, 186−193.
(8) Krebs, C.; Fujimori, D. G.; Walsh, C. T.; Bollinger, J. M. *Acc. Chem. Res.* **2007**, *40*, 484−492.
(9) Tinberg, C. E.; Lippard, S. J. *Acc. Chem. Res.* **2011**, *44*, 280−288.
(10) Puri, M.; Que, L. *Acc. Chem. Res.* **2015**, *48*, 2443−2452.
(11) Nam, W. *Acc. Chem. Res.* **2015**, *48*, 2415−2423.
(12) Seo, M. S.; Kim, N. H.; Cho, K.-B.; So, J. E.; Park, S. K.; Clémancey, M.; Garcia-Serres, R.; Latour, J.-M.; Shaik, S.; Nam, W. *Chem. Sci.* **2011**, *2*, 1039−1045.
(13) Biswas, A. N.; Puri, M.; Meier, K. K.; Oloo, W. N.; Rohde, G. T.; Bominaar, E. L.; Münck, E.; Que, L. *J. Am. Chem. Soc.* **2015**, *137*, 2428−2431.
(14) Shaik, S.; Cohen, S.; Wang, Y.; Chen, H.; Kumar, D.; Thiel, W. *Chem. Rev.* **2010**, *110*, 949−1017.
(15) Chakrabarty, S.; Austin, R. N.; Deng, D.; Groves, J. T.; Lipscomb, J. D. *J. Am. Chem. Soc.* **2007**, *129*, 3514−3515.
(16) Neibergall, M. B.; Stubna, A.; Mekmouche, Y.; Münck, E.; Lipscomb, J. D. *Biochemistry* **2007**, *46*, 8004−8016.
(17) Barry, S. M.; Challis, G. L. *ACS Catal.* **2013**, *3*, 2362−2370.
(18) de Oliveira, F. T.; Chanda, A.; Banerjee, D.; Shan, X.; Mondal, S.; Que, L.; Bominaar, E. L.; Münck, E.; Collins, T. J. *Science* **2007**, *315*, 835−838.
(19) Ghosh, M.; Singh, K. K.; Panda, C.; Weitz, A.; Hendrich, M. P.; Collins, T. J.; Dhar, B. B.; Gupta, S. Sen *J. Am. Chem. Soc.* **2014**, *136*, 9524−9527.
(20) Mills, M. R.; Weitz, A. C.; Hendrich, M. P.; Ryabov, A. D.; Collins, T. J. *J. Am. Chem. Soc.* **2016**, *138*, 13866−13869.
(21) Kundu, S.; Thompson, J. V. K.; Shen, L. Q.; Mills, M. R.; Bominaar, E. L.; Ryabov, A. D.; Collins, T. J. *Chem. - Eur. J.* **2015**, *21*, 1803−1810.
(22) Shen, L. Q.; Kundu, S.; Collins, T. J.; Bominaar, E. L. *Inorg. Chem.* **2017**, *56*, 4347−4356.
(23) Collins, T. J.; Ryabov, A. D. *Chem. Rev.* **2017**, *117*, 9140−9162.
(24) Van Heuvelen, K. M.; Fiedler, A. T.; Shan, X.; De Hont, R. F.; Meier, K. K.; Bominaar, E. L.; Münck, E.; Que, L. *Proc. Natl. Acad. Sci. U. S. A.* **2012**, *109*, 11933−11938.
(25) Oloo, W. N.; Que, L. *Acc. Chem. Res.* **2015**, *48*, 2612−2621.
(26) Olivo, G.; Cussó, O.; Borrell, M.; Costas, M. *JBIC, J. Biol. Inorg. Chem.* **2017**, *22*, 425−452.
(27) Olivo, G.; Cussó, O.; Costas, M. *Chem. - Asian J.* **2016**, *11*, 3148−3158.
(28) Bryliakov, K. P.; Talsi, E. P. *Coord. Chem. Rev.* **2014**, *276*, 73−96.
(29) Chen, K.; Que, L. *J. Am. Chem. Soc.* **2001**, *123*, 6327−6337.
(30) Mas-Balleste, R.; Que, L. *J. Am. Chem. Soc.* **2007**, *129*, 15964−15972.
(31) Bassan, A.; Blomberg, M. R. A.; Siegbahn, P. E. M.; Que, L. *J. Am. Chem. Soc.* **2002**, *124*, 11056−11063.
(32) Hitomi, Y.; Arakawa, K.; Funabiki, T.; Kodera, M. *Angew. Chem., Int. Ed.* **2012**, *51*, 3448−3452.
(33) Chow, T. W. S.; Wong, E. L. M.; Guo, Z.; Liu, Y.; Huang, J. S.; Che, C. M. *J. Am. Chem. Soc.* **2010**, *132*, 13229−13239.
(34) Tse, C. W.; Chow, T. W. S.; Guo, Z.; Lee, H. K.; Huang, J. S.; Che, C. M. *Angew. Chem., Int. Ed.* **2014**, *53*, 798−803.
(35) Lyakin, O. Y.; Zima, A. M.; Samsonenko, D. G.; Bryliakov, K. P.; Talsi, E. P. *ACS Catal.* **2015**, *5*, 2702−2707.
(36) Lyakin, O. Y.; Prat, I.; Bryliakov, K. P.; Costas, M.; Talsi, E. P. *Catal. Commun.* **2012**, *29*, 105−108.
(37) Oloo, W. N.; Meier, K. K.; Wang, Y.; Shaik, S.; Münck, E.; Que, L. *Nat. Commun.* **2014**, *5*, 3046.
(38) Makhlynets, O. V.; Oloo, W. N.; Moroz, Y. S.; Belaya, I. G.; Palluccio, T. D.; Filatov, A. S.; Müller, P.; Cranswick, M. A.; Que, L.; Rybak-Akimova, E. V. *Chem. Commun.* **2014**, *50*, 645−648.

DOI: 10.1021/jacs.7b11400
J. Am. Chem. Soc. XXXX, XXX, XXX−XXX

(39) Chen, M. S.; White, M. C. *Science* **2007**, *318*, 783−787.
(40) Gómez, L.; Garcia-Bosch, I.; Company, A.; Benet-Buchholz, J.; Polo, A.; Sala, X.; Ribas, X.; Costas, M. *Angew. Chem., Int. Ed.* **2009**, *48*, 5720−5723.
(41) Ortiz De Montellano, P. R. *Chem. Rev.* **2010**, *110*, 932−948.
(42) Rittle, J.; Green, M. T. *Science* **2010**, *330*, 933−937.
(43) Serrano-Plana, J.; Oloo, W. N.; Acosta-Rueda, L.; Meier, K. K.; Verdejo, B.; García-España, E.; Basallote, M. G.; Münck, E.; Que, L.; Company, A.; Costas, M. *J. Am. Chem. Soc.* **2015**, *137*, 15833−15842.
(44) Serrano-Plana, J.; Aguinaco, A.; Belda, R.; García-España, E.; Basallote, M. G.; Company, A.; Costas, M. *Angew. Chem., Int. Ed.* **2016**, *55*, 6310−6314.
(45) Wang, Y.; Janardanan, D.; Usharani, D.; Han, K.; Que, L.; Shaik, S. *ACS Catal.* **2013**, *3*, 1334−1341.
(46) Jackson, T. A.; Rohde, J.-U.; Seo, M. S.; Sastri, C. V.; DeHont, R.; Stubna, A.; Ohta, T.; Kitagawa, T.; Münck, E.; Nam, W.; Que, L., Jr. *J. Am. Chem. Soc.* **2008**, *130*, 12394−12407.
(47) Lim, M. H.; Rohde, J.; Stubna, A.; Bukowski, M. R.; Costas, M.; Ho, R. Y. N.; Munck, E.; Nam, W.; Que, L. *Proc. Natl. Acad. Sci. U. S. A.* **2003**, *100*, 3665−3670.
(48) Schulz, C. E.; Rutter, R.; Sage, J. T.; Debrunner, P. G.; Hager, L. P. *Biochemistry* **1984**, *23*, 4743−4754.
(49) Roberts, J. E.; Hoffman, B. M.; Rutter, R.; Hager, L. P. *J. Am. Chem. Soc.* **1981**, *103*, 7654−7656.
(50) Klein, J. E. M. N.; Que, L. In *Encyclopedia of Inorganic and Bioinorganic Chemistry*; John Wiley & Sons, Ltd: Chichester, 2016; pp 1−22.
(51) Pattanayak, S.; Jasniewski, A. J.; Rana, A.; Draksharapu, A.; Singh, K. K.; Weitz, A.; Hendrich, M.; Que, L.; Dey, A.; Sen Gupta, S. *Inorg. Chem.* **2017**, *56*, 6352−6361.
(52) Prakash, J.; Rohde, G. T.; Meier, K. K.; Münck, E.; Que, L. *Inorg. Chem.* **2015**, *54*, 11055−11057.
(53) Frisch, J. R.; Vu, V. V.; Martinho, M.; Münck, E.; Que, L. *Inorg. Chem.* **2009**, *48*, 8325−8336.
(54) Chanda, A.; Shan, X.; Chakrabarti, M.; Ellis, W. C.; Popescu, D. L.; De Oliveira, F. T.; Wang, D.; Que, L.; Collins, T. J.; Münck, E.; Bominaar, E. L. *Inorg. Chem.* **2008**, *47*, 3669−3678.
(55) Vrajmasu, V.; Munck, E.; Bominaar, E. L. *Inorg. Chem.* **2003**, *42*, 5974−5988.
(56) Sinnecker, S.; Neese, F.; Noodleman, L.; Lubitz, W. *J. Am. Chem. Soc.* **2004**, *126*, 2613−2622.
(57) Cernak, T.; Dykstra, K. D.; Tyagarajan, S.; Vachal, P.; Krska, S. W. *Chem. Soc. Rev.* **2016**, *45*, 546−576.
(58) Bigi, M. A.; Reed, S. A.; White, M. C. *Nat. Chem.* **2011**, *3*, 216−222.
(59) Bigi, M. A.; Reed, S. A.; White, M. C. *J. Am. Chem. Soc.* **2012**, *134*, 9721−9726.
(60) Shugrue, C. R.; Miller, S. J. *Chem. Rev.* **2017**, *117*, 11894−11951.
(61) Oloo, W. N.; Fielding, A. J.; Que, L. *J. Am. Chem. Soc.* **2013**, *135*, 6438−6441.
(62) Oloo, W. N.; Banerjee, R.; Lipscomb, J. D.; Que, L. *J. Am. Chem. Soc.* **2017**, *139*, 17313−17326.
(63) Zima, A. M.; Lyakin, O. Y.; Bryliakov, K. P.; Talsi, E. P. *Catal. Commun.* **2018**, *108*, 77−81.
(64) Costas, M.; Mehn, M. P.; Jensen, M. P.; Que, L. *Chem. Rev.* **2004**, *104*, 939−986.
(65) Harman, D. G.; Ramachandran, A.; Gracanin, M.; Blanksby, S. J. *J. Org. Chem.* **2006**, *71*, 7996−8005.
(66) Standard Guide for Raman Shift Standards for Spectrometer Calibration. *ASTM Int.* 2002, *96* (Reapproved 2007), 1−11.
(67) Menges, F. *Spekwin32 - optical spectroscopy software*, Version 1.72.0, 2015, http://www.effemm2.de/spekwin.

DOI: 10.1021/jacs.7b11400
J. Am. Chem. Soc. XXXX, XXX, XXX−XXX